JMEPEG (2024) 33:2562–2571
https://doi.org/10.1007/s11665-023-08887-1

1059-9495/$19.00

ORIGINAL RESEARCH ARTICLE

Formation, Transformation, and Electrical Performance of Magnéli Phases Obtained by Flame Spraying from TiO_2 Particles

F. Vargas-Galvis, J.D. Holguín-Villa, J.A. Arias Gómez, A.F. Mejía, A.A. Velásquez, M. Arroyave, and C.C. Palacio Espinosa

Submitted: 10 February 2023 / Revised: 18 September 2023 / Accepted: 8 October 2023 / Published online: 30 November 2023

In this paper, the formation and transformation of Magnéli phases (Ti_nO_{2n-1}) during manufacturing of flame-sprayed coatings from two powders consisting of anatase nanoparticles and submicrometric particles with Magnéli phases is analyzed, respectively. These powders were thermally sprayed on a ceramic substrate through oxidizing and neutral flame. Crystalline phases in powders and coatings were identified by x-ray diffraction and quantified by the Rietveld method, verifying the presence of identified crystalline phases in coatings by x-ray photoelectron spectroscopy. Finally, the electrical conductance of coatings was measured by the four-point probe method. Results indicate that Magnéli phases are produced from anatase nanoparticles sprayed using both the oxidizing and neutral flames, and when the neutral flame and finest particles are used, a high quantity of Ti_4O_7 and Ti_5O_9, recognized thanks to their high electrical conductivity, is obtained. In contrast, when the coatings were fabricated from the powder containing Magnéli phases, they were oxidized as much in oxidizing as in neutral flame, producing a partial transformation from Ti_4O_7 and Ti_5O_9 to both the rutile phase and TiO in low quantity. In spite of this partial transformation, the coatings maintain high electrical conductivity thanks to Ti_4O_7 and Ti_5O_9 Magnéli phases remaining and the TiO produced.

Keywords ceramic coatings, electrical behavior, flame spraying process, Magnéli phases, titanium dioxide

1. Introduction

Magnéli phases are sub-stoichiometric titanium oxides with a general formula Ti_nO_{2n-1}, where n is between 4 and 10 (Ref 1). They were discovered by Arne Magnéli in the middle of the past century, and recent advances in materials science have made evident their high conductivity and chemical resistance (Ref 2). The Ti_4O_7, which is the most conductive of the Magnéli phases, can be as conductive as graphite (Ref 3). These types of titanium suboxides have versatile magnetic and optical characteristics (Ref 4). These properties make materials composed of Magnéli phases ideal for the fabrication of electrodes and battery parts, fuel cells, among many others (Ref 5).

The aforementioned contributes to enriching the list of strengths of titanium dioxide (TiO_2), which already has evidenced properties as important as its super-hydrophilic ability, self-cleaning, antibacterial properties, and its role as a heterogeneous photocatalysis promoter under UV light for air and water remediation (Ref 6). Some authors consider Magnéli phases essential for future technological developments and advancements in electronic devices (Ref 4). Current technological challenges for these materials focus on improving synthesis processes to achieve stable Magnéli phases and enable their industrial scalability (Ref 5, 7-18).

Traditional synthesis methods for those titanium suboxides are based on reduction reactions of TiO_2 under controlled atmospheres, temperatures ranging between 850 and 1300 °C, and dwell times from 3 h to 1 week (Ref 13, 19, 20). These reduction reactions can be classified depending on the reducing reagent used as follows: (i) carbothermal synthesis which uses black carbon (Ref 21) or the by-product of organic compounds degradation, such as PVA, as the source of the carbon to be used as a reducing reagent to produce Ti_nO_2n-1 phases (n = 2, 3, 5, 6, and 9) (Ref 4) in processes conducted under vacuum conditions or inert atmospheres, (ii) reduction by thermal treatment using hydrogen as reducing reagent, which is usually obtained from ammonia decomposition (Ref 3) or provided as element blended with an inert gas (Ref 5, 10), (iii) metallothermic reduction using high potential reductive metals as reducing reagents such as aluminum, magnesium, calcium, sodium, or titanium (Ref 4, 20), (iv) hydrothermal synthesis using $TiCl_3$ as precursor and L-ascorbic acid as reductive reagents (Ref 22), (v) sol–gel synthesis from titanium tetrabutoxide as precursor (Ref 23), and (vi) electrochemical reduction using titanium as anode and a carbon rod as cathode immersed in an 0.3 wt.% NH4F electrolyte (Ref 18).

There are also reports of titanium suboxides films containing Magnéli phases, such as Ti_3O_5 and Ti_4O_7, fabricated by physical vapor deposition (PVD) from a metallic titanium target

F. Vargas-Galvis, J.D. Holguín-Villa, and **J.A. Arias Gómez**, GIPIMME and GIMACYR Research Groups, Department of Materials Engineering, University of Antioquia, Street 67 # 53-108, 050010 Medellín, Colombia; **A.F. Mejía, A.A. Velásquez, M. Arroyave,** and **C.C. Palacio Espinosa**, GEMA Research Group, Applied Sciences and Engineering School, University EAFIT, Street 49 # 7 sur-50, 050022 Medellín, Colombia. Contact e-mail: fabio.vargas@udea.edu.co.

under a poor oxygen atmosphere (Ref 4). Thermal spraying processes have also made their contributions to the Magnéli phases production (Ref 24), as it was reported by Ctibor, et al. (Ref 25, 26) and Jaramillo, et al. (Ref 27) who obtained this kind of phases in coatings fabricated through plasma spraying from commercial TiO_2 powders (Ref 25-27).

The importance of introducing H_2 into the plasma jet as a reductive reagent was documented by Berger (Ref 28), who reported the formation of Magnéli phases in atmospheric plasma spraying (APS) and high-velocity oxygen fuel (HVOF) processes. Recently, APS was used to synthesize nanosized particles of typical titanium suboxides (Ti_4O_7 and Ti_5O_9) from commercial metatitanic acid (H_2TiO_3) powders in argon and Ar/H_2 plasmas. The raw materials were sprayed inside a cooling chamber and subsequently filtered. It was found that an increase in H_2 favored the formation of Magnéli phases (Ti_nO_{2n-1}, where $n \leqq 3$) (Ref 29). Peña, et al. (Ref 30) manufactured thermally sprayed coatings through a highly oxidative oxyacetylene flame from a titanium suboxides powder finding out that Magnéli phases present in the coatings were richer in oxygen than the phases observed in the raw powders. According to the above, it can be noted that the atmosphere (gases and temperature) in which particles are sprayed promotes the loss of oxygen to reduce titanium dioxide (TiO_2), producing Magnéli phases. However, under proper atmospheric conditions, it is also possible for those suboxides to be oxidized, resulting in the production of titanium dioxide.

This background evidence indicates that thermal spraying processes provide alternative methods for obtaining titanium suboxides directly in coatings on a wide range of surfaces, in less time than traditional methods. Furthermore, in the case of oxyacetylene flame spraying, as proposed in this paper, it can be done at a low cost. Considering the information mentioned above, this research was conducted to evaluate both the effect of oxyacetylene flame type and the particle sizes on the formation and transformation of Magnéli phases during the manufacture of thermally sprayed coatings, with potential electrical applications.

2. Materials and Methods

In order to study the formation and transformation of Magnéli phases by flame spraying process, two titania powders were used as feedstock. The first of them consisted on an 18-nm average particle size powder fabricated by the US Research Nanomaterials (US-RN), which was agglomerated in the laboratory by pelletization method in order to obtain granules of micrometric size distribution. The granules obtained were dried at room temperature and sieved to extract three different particle size fractions: 45-75 μm, 75-106 μm, and 75-150 μm that were named as fine, medium, and coarse, respectively. Since the granules obtained by pelletization are sufficiently compacted, and therefore, their mechanical strength is enough to be used as feedstock in the manufacture of thermally sprayed coatings, they do not require sintering heat treatment after agglomeration (Ref 31). The other powder used was Oerlikon Metco 6231A™ (OM 6231A) which, according to the manufacturer's description, is agglomerated and sintered (Ref 32). The agglomeration is accomplished by the spray-drying process (Ref 33). The particle size distribution of this powder was determined by laser diffraction (LD) with a Malvern Master Sizer 2000 equipment.

Granules obtained by pelletization of the US-RN nanoparticles and OM 6231A powders were tested by wavelength-dispersive x-ray fluorescence (WD-XRF) using a Thermo Fisher SCIENTIFIC ARL™ OPTIM'X spectrometer to determine their chemical composition. Crystalline phases of the powders and sprayed coatings were identified by x-ray diffraction (XRD) with the PANalytical X'pert High Score software from the results obtained with an x-ray diffractometer of the commercial brand Malvern-PANalytical Model Empyrean 2012. The XRD diffractometer has a three-dimensional detector, with a Co (1.79 nm) source operating at 40 kV and 40 mA for the US-RN nanoparticles and Cu source (1.54 nm) operating at 45 kV and 40 mA for OM 6231A powder and coatings. The tests were carried out using steps each 0.05° and time per step of 52 s. The results obtained with the cobalt source were converted to their equivalents for the copper source.

Phases quantifications were carried out by the Rietveld method using the Material Analysis Using Diffraction—MAUD software. The code of each one of standards used to identify and quantify the crystalline phases in powders was: COD 96-900-9087 and COD 96-901-4170 for anatase phase and sulfur, respectively, in the US-RN, as well as, the ICSD 01-076-1690 and COD 96-100-8049 were used for Ti_5O_9 and Ti_4O_7, respectively, in OM 6231A. Additionally, the standard used to coatings was: ICOD 01-071-1169, COD 96-101-0943, and COD 96-900-8214 for anatase phase, ICOD 01-077-0441, ICSD 98-002-4277, ICSD 98-016-5923, COD 96-900-1682, and COD 96-900-9084 for rutile phase, COD 96-152-0784 for Ti_9O_{17}, COD 96-100-8197 for Ti_7O_{13}, ICOD 01-076-1690 for Ti_5O_9, COD 96-152-7760, ICOD 01-072-1722, and ICSD 98-001-6297 for Ti_4O_7, ICSD 98-007-5193 for Ti_3O_5, and ICOD 01-073-1117 for Ti_3O.

The chemical composition and the local bonding of the titanium atoms in the coatings were verified using an x-ray photoelectron spectrometer (NAP-XPS) Specs brand, equipped with a PHOIBOS 150 1D-DLD analyzer and a monochromatic Al-Kα (1486.7 eV, 13 kV, 100 W) source. The analyses were performed with step energy of 86.6 eV for the general spectra and 20 eV for the high-resolution spectra, the step was 1 eV for the general spectra and 0.1 eV for the high-resolution spectra. Prior to measuring the XPS data, the sample surface was cleaned by *in situ* Ar + ion etching for 600 s at a gun ion energy of 5 keV to remove surface contaminants that accumulated on the coatings during handling. Five cycles of analysis were performed for the general spectra and 20 cycles for the high-resolution spectra. The spectrometer was calibrated using the Ag-3d5/2 peak at 368.53 eV. XPS high-resolution peaks were de-convoluted by a fitting routine including Shirley background subtraction and mixed Gauss–Lorentz function (using CasaXPS software). Scofield relative sensitivity factors were used to correct the atomic percentages calculations.

On the other hand, the powders' morphology and coatings structure were analyzed by scanning electron microscopy (SEM) using a JEOL JSM-6490LV microscope.

Agglomerated granules of the US-RN nanoparticles and OM 6231A powder were flame-sprayed on a silico-aluminous ceramic substrate using a Eutectic Terodyn 2000™ torch. The coatings were manufactured setting the spray parameters determined from previous experiments such as the kind of flame produced by the torch through the combustion gases ratio, spraying distance, speed between the torch and the substrate, and the powders' flow rate. Two kinds of flames were

Table 1 Flame spraying parameters

Feedstock powder	Flame type	Particle size fraction	Spraying distance [cm]	Sample code
A: US-RN Pelletized	Oxidizing	Medium	7.5	$A_{O\text{-}m7.5}$
	Neutral	Coarse		$A_{N\text{-}c7.5}$
		Medium		$A_{N\text{-}m7.5}$
		Fine		$A_{N\text{-}f7.5}$
B: OM 6231A	Neutral	Fine–medium	9.0	$B_{N\text{-}f\text{-}m9}$
	Oxidizing	Fine–medium		$B_{O\text{-}f\text{-}m9}$

used to manufacture the coatings: (i) An oxidizing flame produced by the 1:2.5 acetylene:oxygen volume ratio, and (ii) a neutral flame produced by 1:1.7 acetylene:oxygen volume ratio. Manufactured coatings were codified according to the sprayed powder (A if the US-RN or B if OM 6231A), the type of flame (O if oxidizing and N if neutral), the particles size fraction (c if particles are coarse, m if they are medium, and f if they are fine), and the spraying distances (7.5 and 9 cm) as it is indicated in Table 1.

The flame types listed in Table 1 were produced by feeding 22 l/min of acetylene at 0.08 MPa into the nozzle of the torch and blended with 37 l/min and 55 l/min of oxygen at 0.34 MPa for the neutral and oxidizing flames, respectively. The substrates used were 25 mm in diameter and 6-mm thick disks extracted from a silico-aluminous brick. These substrates were positioned in front of the torch at the specified spraying distance mentioned in Table 1. Prior to the spraying process, the substrates were preheated to approximately 350 °C by passing the flame in front of them while they rotated at a speed of 116 rpm. Feedstock powder was injected into the flame using a nitrogen stream of 17 L/min at a pressure of 0.27 MPa as the carrier gas. This process resulted in feedstock powders spraying at a relative speed with respect to the substrates of 0.59 cm/s for 250 s, performing 10 passes of the torch in front of the substrates (four preheat and six spraying passes), to cover a surface of 344.8 cm^2 with a layer of 153 ± 36.8 micrometers.

The electrical resistance (R) of coatings was measured on their surface by four-point probe method by applying ramps of direct current (DC) between 0 and 2 μA in steps of 0.1 μA using a KEITHLEY 6221 programmable current source, with a sensitivity from 100 fA in a range from 4 pA to 210 mA. The voltage responses were measured using a KEITHLEY 2182A programmable nanovoltmeter, which is capable of reliably and reproducibly measuring signals ranging from 1 nV to 100 V. To conduct the measurements, four short copper wires were attached with silver paint to points located near the edge of each coating, forming the corners of a rectangle. Current was applied through two of the wires, while voltage was measured across the two opposite wires. This procedure was performed for two samples of each coating. The slope of the curve that describes the relationship between the voltage and current signals corresponds to the electrical resistance of the coating, as governed by Ohm's law.

Finally, the manufactured coatings were embedded in an epoxy resin and cut using a Buehler 15 LC diamond blade to obtain cross-sections. These cross-sections were then ground and polished following the ASTM E1920-03 (2021) standard to prepare them for observation of the coating's structure by SEM. The results of this observation will be presented in section 3.2.

3. Results

3.1 Feedstock Powders

According to the results of chemical compositions conducted by XRF on the US-RN nanoparticles and OM 6231A powder, as presented in Table 2, it was possible to determine that the feedstock powders used for manufacturing the coatings consisted primarily of TiO_2, along with other compounds such as CuO, CaO, P_2O_5, and NiO. In the US-RN nanoparticles, some traces of SO_3 were also detected.

Crystalline phases identified by XRD in the feedstock powders are shown in Fig. 1, and their respective compositions are presented in Table 2. It is evident from this table that the US-RN nanoparticles primarily consist of anatase with low quantities of other compounds such as sulfur oxide and non-crystalline TiO_2. On the other hand, the OM 6231A powder is composed of Ti_4O_7 and Ti_5O_9 phases, which correspond to titanium suboxides known as Magnéli phases (Ref 1).

Sigma and R_{exp} quality factors obtained for the Rietveld analysis XRD are 1.4 and 2.7, respectively, for the US-RN nanoparticles while they are 1.4 and 3.2 for the OM 6231A powder. These values indicate highly reliable results for the quantification of crystallographic phases in the analyzed powders since they are below 2 for sigma and below 15 for R_{exp} (Ref 34, 35).

Moreover, the morphological analyses conducted on the granules obtained by pelletization from the US-RN nanoparticles and the OM 6231A powder revealed that they have a rounded shape, and their size distributions are in the micrometric range. Furthermore, it was observed that each granule of these powders is composed of small particles. In the case of the granules obtained from the US-RN nanoparticles, these small particles are in the nanometric range. For the OM 6231A powder, the small particles are submicrometric and exhibit evidence of sintering necks, as depicted in Fig. 2.

Regarding to particle size distribution analysis carried out to OM 6231A powder, the results indicate that the d_{10}-d_{90} interval corresponds to 44.9-102.5 μm. This particle size distribution covers both the fine and medium fractions (45-75 μm and 75-106 μm) obtained by sieving for pelletized granules from the US-RN. Despite TiO_2 could be present as anatase, rutile, or brookite (Ref 36), others researchers indicated that anatase appears as a stable phase when the particle size is smaller than a critical size (6.9 ∼ 22.7 nm) (Ref 37-39).

The aforementioned elucidates why the TiO_2 granules obtained through pelletization from the US-RN nanoparticles, with an average particle size of 18 nm, predominantly consisted of the anatase phase, accounting for 98.8 wt.% of the composition. In contrast, the presence of Ti_4O_7 and Ti_5O_9 Magnéli phases in the granules of OM 6231A suggests that these phases might have been formed during the sintering process employed to bind the submicrometric particles that constitute them.

3.2 Manufactured Coatings

SEM results obtained from the observation of the cross-sections of the manufactured coatings indicate that their structures are composed of lamellae, pores, and cracks. These features are typical characteristics of thermally sprayed coatings (Ref 24, 40). Despite the use of two different TiO2 powders with varying particle size fractions, two types of oxyacetylene

Table 2 Chemical composition and phases of feedstock powders used to manufacture the coatings samples

Feedstock powders	Chemical composition, wt.%			Phases content, wt.%			
	TiO_2	SO_3	Others	TiO_2 anatase	Sulfur oxide[1]	Ti_4O_7	Ti_5O_9
US-RN	99.23±0.04	O.38±0.02	0.39	98.8 ±0.0	1.2 ±0.2	…	…
OM 6231A	99.91±0.02	…	0.09	…	…	58.48 ±5.69	41.51 ± 0.0

[1]This phase includes low quantities of other non-crystalline oxides, including TiO_2

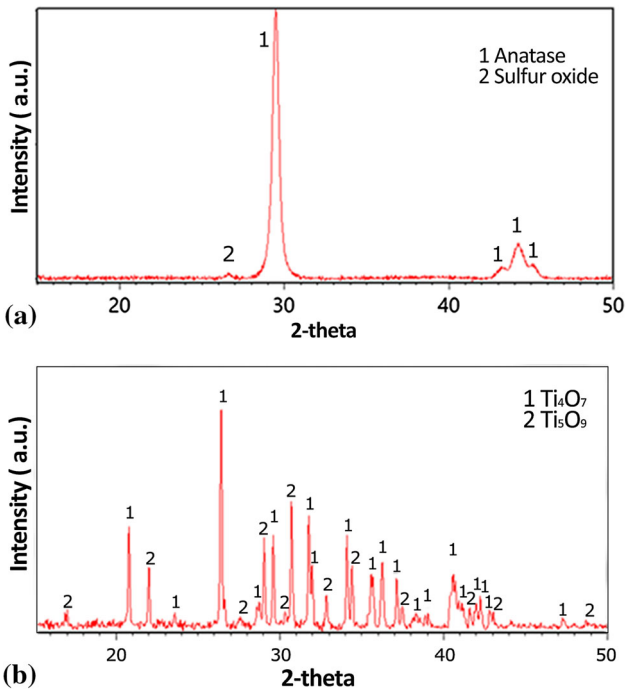

Fig. 1 XRD patterns obtained for the feedstock powders. (a) US-RN. (b) OM 6231A

flames, and two different thermal spraying distances, as specified in Table 1, no significant changes were observed in the structure of the six manufactured coatings. Figure 3 illustrates the representative structure of the manufactured coatings.

The results of phases identification and quantification in each coating are shown in Table 3.

Both sig. and R_{exp} Rietveld quality factors are ranged between 1.6 and 2.0 and between 3.2 and 3.8, respectively. The above indicates that the values reported in Table 3 are reliable, since the criteria established for the goodness of fitting for Rietveld refinements performed with MAUD are sig. < 2 and $R_{exp} < 15$ (Ref 34, 35). The high values of standard deviation calculated for some of the phases can be attributed to their low crystallinity. In this table, the crystalline phases are presented from top to bottom in decreasing order of O/Ti ratio from the most oxidized (TiO_2, in anatase and rutile phases, with an O/Ti ratio of 2), to the most reduced (Ti_3O, with an O/Ti ratio of 0.3).

The results of the XRD analyses reveal that the TiO_2 in the form of anatase phase present in the US-RN agglomerated powder undergoes transformation during the manufacturing of the coatings using the oxyacetylene flame. This transformation leads to the formation of both TiO_2 rutile and Magnéli phases of the type Ti_nO_{2n-1}, as depicted in Fig. 4. Specifically, the Magnéli phases produced in the coating manufactured using the oxidizing flame were Ti_9O_{17} and Ti_7O_{13}, whereas in the coatings sprayed with the neutral flame, the Magnéli phases observed were Ti_7O_{13}, Ti_4O_7, and even Ti_3O.

The deconvoluted high-resolution XPS spectrum of $A_{N\text{-}f7.5}$ sample, which is representative of coatings manufactured from the US-RN agglomerated powder, showed three contributing peaks in the Ti $2p_{3/2}$ region shifted to higher binding energy accompanied by a broadening, which reveals the formation of Ti-O bonds, as it is shown in Fig. 5a. The two main peaks, located at 457.02 eV and 457.44 eV, correspond to Ti^{+3} in Ti_2O_3 (Ref 41-43) and Ti_4O_7 (Ref 20). The third peak at 457.96 eV is assignable to Ti^{+4} in TiO_2 rutile phase (Ref 43). As the binding energy is shifted to higher energy, higher oxidation level is observed in the formation of the titanium oxide compounds in the coatings. High-resolution peaks in the O1s region (not shown here) shifted in the binding energy confirm to the formation of these Ti-O bonds.

Moreover, the results obtained for the coatings sprayed from the OM 6231A powder indicate that a portion of the Ti_4O_7 and Ti_5O_9 Magnéli phases present in the feedstock particles underwent an oxidation process, resulting in the production of TiO_2 in the rutile phase.

In addition, the Magnéli phases that were present in the raw material and that did not undergo transformation, as well as low amounts of Ti_3O_5 and Ti_3O, were detected in these coatings as it is shown in Fig. 6.

The spin-orbit splitting of the Ti2p peak can potentially overlap with compounds of a high oxidation state, resulting in a complex XPS spectrum. This effect was observed in the deconvoluted high-resolution XPS spectrum of the $B_{O\text{-}f\text{-}m9}$ sample, as shown in Fig. 5b. However, the binding energies of the main peaks in the spectra can be assigned to various titanium oxide phases, which is representative of coatings manufactured from OM 6231A powder. The shifted main peak in the Ti $2p_{3/2}$ region is located at 456.5 eV, and it is assignable to Ti^{+3} in Ti_2O_3 (Ref 44). Additionally, a peak at 458.6 eV corresponds to Ti^{+4} of rutile TiO_2 was identified (Ref 42-44). Other peaks detected at lower binding energy (454.9 eV, 454.2 eV, and 452.8 eV) are assignable to Ti^0 and Ti^{+2} from metallic titanium and TiO, respectively (Ref 45, 46). As it was previously mentioned, the simultaneous presence of Ti^{+3} and Ti^{+4}, corresponding to Ti_2O_3 and TiO_2 rutile, respectively, could be indicative of Ti_4O_7 occurrence, since the crystalline structure of this Magnéli phase is composed by rutile blocks interleaved with corundum-like Ti_2O_3 layers (Ref 20, 41, 42). The TiO identified from the XPS analysis may be present in amounts below the detectable limits by XRD.

Finally, the results of electrical behavior of manufactured coatings are shown in Fig. 7 and Table 3.

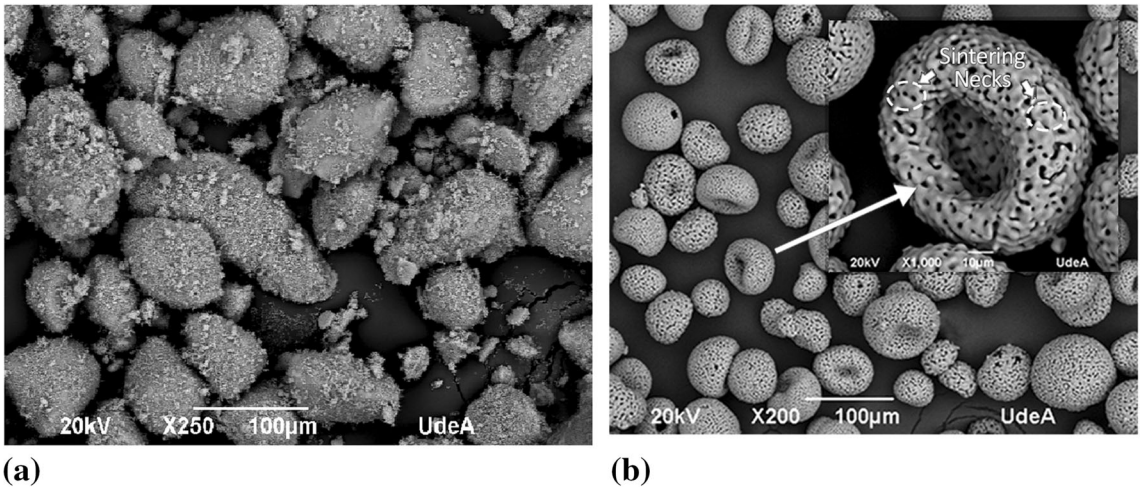

Fig. 2 Morphology of granules used as feedstock to manufacture the TiO_2 coatings. (a) US-RN. (b) OM 6231A

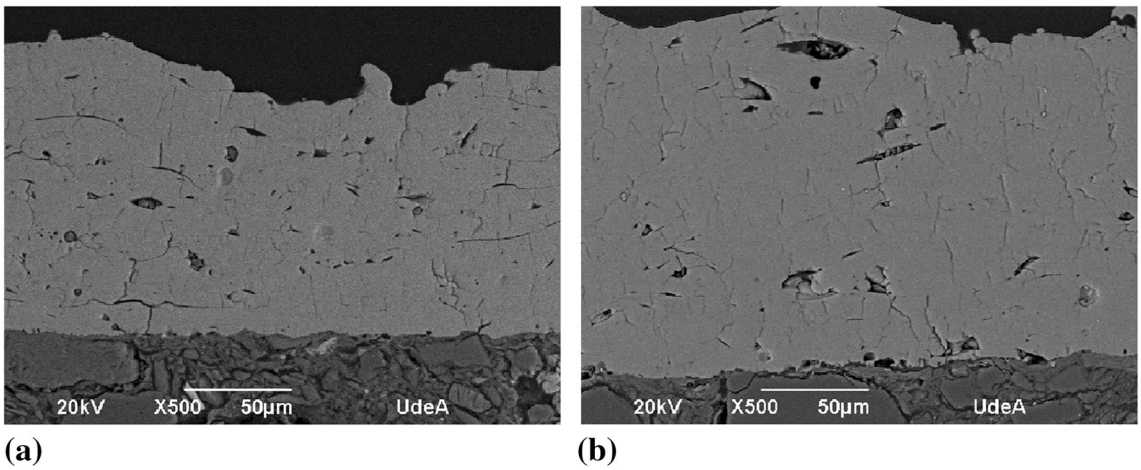

Fig. 3 Characteristic structure of the TiO_2 coatings manufactured. (a) $A_{O\text{-}m7.5}$ sample. (b) $B_{O\text{-}f\text{-}m9}$ sample

Table 3 Results of the quantification of phases and electrical resistance of the manufactured coatings

	Sample code	$A_{O\text{-}m7.5}$	$A_{N\text{-}c7.5}$	$A_{N\text{-}m7.5}$	$A_{N\text{-}f7.5}$	$B_{N\text{-}f\text{-}m9N}$	$B_{O\text{-}fm9}$
Crystalline phases content (wt. %)	TiO_2 (anatase)	…	2.1±0.0	0.5±0.0	0.3±0.2	…	…
	TiO_2 (rutile)	10.6±0.0	19.8±1.4	17.2±2.6	26.6±0.0	1.8±0.0	20.1±0.0
	Ti_9O_{17}	31.9±2.9	…	…	…	…	…
	Ti_7O_{13}	57.5±4.2	78.1±9.1	82.3±12.3	…	…	…
	Ti_5O_9	…	…	...	…	35.8±3.1	28.2±1.2
	Ti_4O_7	…	…	…	72.3 ± 2.9	52.7±3.6	50.4±1.4
	Ti_3O_5	…	…	…	…	1.9±0.5	0.8±0.3
	Ti_3O	…	…	…	0.8±0.1	0.8±0.2	0.4±0.1
Rietveld fitting parameters	Sig.	1.9	1.8	2.0	2.0	1.6	1.8
	R_{exp}	3.7	3.2	3.2	3.4	3.8	3.8
Electrical resistance, Ω		13.3±0.5	5.4±0.1	4.5±0.1	3.6±0.0	2.1±0.0	1.6±0.1

4. Discussion

According to the results of phase identification and quantification, it has been determined that in the coatings manufactured using the US-RN powder, the rutile phase is produced through the transformation of the anatase phase present in these feedstock particles. This transformation occurs upon heating from 400 °C (Ref 47, 48). Furthermore, the Magnéli phases identified in the coatings manufactured using both the oxidizing flame (Ti_9O_{17} and Ti_7O_{13}) and the neutral flame (Ti_7O_{13} and

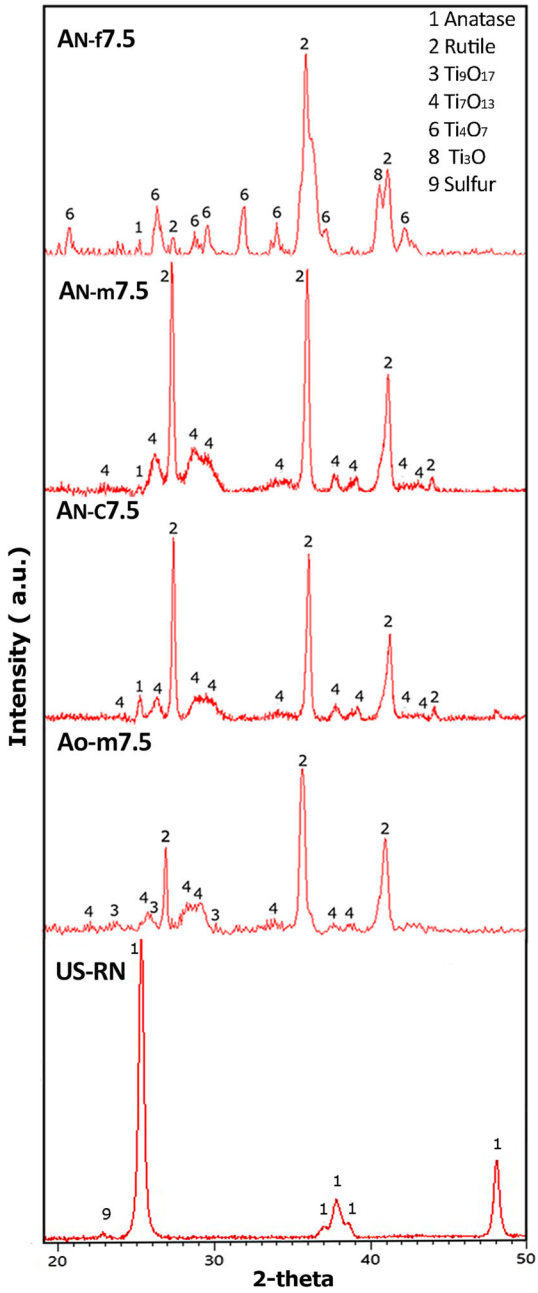

Fig. 4 XRD patterns of the US-RN nanoparticles and the coatings sprayed from them

Ti_4O_7), as well as the small amount of Ti_3O in the latter, are formed due to the reducing effect of both hydrogen and carbon monoxide present in the oxyacetylene flame used for spraying.

Oxyacetylene flames used in the thermal spraying process are produced in two stages. In the first stage, regardless of whether the flame is oxidizing or neutral, an equimolar mixture of acetylene and oxygen reacts, generating the primary zone of the flame with an inner light blue cone. In this zone, carbon monoxide and hydrogen are formed according to Reaction 1 (Ref 40, 49, 50).

$$2C_2H_2 + 2O_2 \rightarrow 4CO + 2H_2 \quad \text{(Eq 1)}$$

The maximal temperature is achieved in the primary zone for a neutral flame, reaching approximately 3170 °C, with a length of 6.8 cm. In contrast, the excess of oxygen added to produce the oxidizing flame does not participate in the chemical reaction mentioned earlier, but it does consume heat for its own warming, thereby reducing the maximum temperature of the primary zone to around 3080 °C. Additionally, the length of the primary zone increases to 7.6 cm in the case of the oxidizing flame (Ref 50, 51).

In the second stage of the reaction, the carbon monoxide and hydrogen gas generated in the primary zone of the flame react with the surrounding oxygen to form the secondary zone of the flame. In this zone, carbon dioxide and water steam are produced according to Reaction 2. The secondary zone of the flame exhibits a plume shape and is characterized as the coldest and least bright region of the flame.

$$4CO + 2H_2 + 3O_2 \rightarrow 4CO_2 + 2H_2O \quad \text{(Eq 2)}$$

The overall result of oxyacetylene combustion produces carbon dioxide and water steam as described in Reaction 3.

$$2C_2H_2 + 5O_2 \rightarrow 4CO_2 + 2H_2O + 1300\ \text{kJ/mol} \quad \text{(Eq 3)}$$

Based on this information, it can be stated that the available oxygen in the oxidizing flame is insufficient to fully oxidize all the carbon monoxide (CO) and hydrogen (H_2) produced in the primary zone of the flame. As a result, some oxygen atoms are derived from the melted TiO_2 particles, leading to the formation of Magnéli phases or titanium suboxides observed in the coatings sprayed using both oxidizing and neutral flames. In the coating sprayed with the oxidizing flame, the O/Ti ratio changes from 2/1 in TiO_2 (anatase phase) present in the feedstock powder to 2/1 in TiO_2 (rutile phase). Additionally, the O/Ti ratios for Magnéli phases are 1.89/1 for Ti_9O_{17} and 1.86/1 for Ti_7O_{13}. In the coatings manufactured using the neutral flame, the O/Ti ratio obtained was 2/1 for TiO_2 in the rutile phase. Furthermore, the O/Ti ratios for Magnéli phases were measured as 1.86/1 for Ti_7O_{13}, 1.75/1 for Ti_4O_7, and 1/3 for Ti_3O. These ratios indicate that in the coatings manufactured using the neutral flame, the TiO_2 reached a higher reduction state compared to the coatings manufactured using the oxidizing flame.

The reduction state of TiO_2 increases with a decrease in the particle size fraction used to spray the coatings. Consequently, when the particle size fraction decreased from coarse to medium in $A_{N\text{-}c7.5}$ and $A_{N\text{-}m7.5}$ samples, the percentage of the Ti_7O_{13} phase increased from 78.1 ± 9.1 to 82.3 ± 12.3 wt.%. Likewise, when finest particles size fraction was used to manufacture the coating ($A_{N\text{-}f7.5}$ sample), a Magnéli phase more reduced (Ti_4O_7) and Ti_3O were obtained.

In addition, the sprayed coatings from coarse powders evidenced some remaining percentage of anatase ($A_{N\text{-}c7.5}$ sample) which reduces its content in coatings as the finest the feedstock powder ($A_{N\text{-}c7.5}$, $A_{N\text{-}m7.5}$, and $A_{N\text{-}f7.5}$ samples) favoring its transformation to rutile and Magnéli phases during the coatings' formation. Magnéli phases formation is regulated by the heating limitations experimented in coarser particles during their flight along the oxyacetylene flame. According to some authors (Ref 40, 52), the speed attained by particles in an oxyacetylene flame can reach up to 60 m/s. As a result, the residence time during their flight along the 7.5 cm spraying distance could be as short as 1.25 ms. As a consequence, the low residence time of particles in the flame poses a limitation for the transformation from anatase to Magnéli phases, particularly for larger particles.

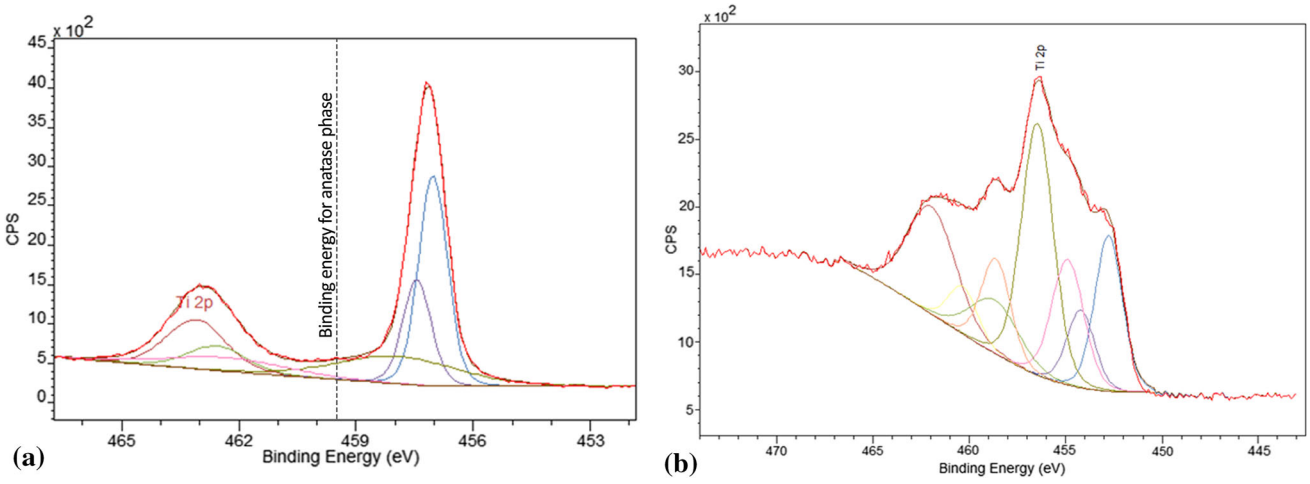

Fig. 5 XPS spectra of representative coatings manufactured from the US-RN and OM 6231A powders. (a) $A_{N\text{-}f7.5}$ coating. (b) $B_{O\text{-}f\text{-}m9}$ coating

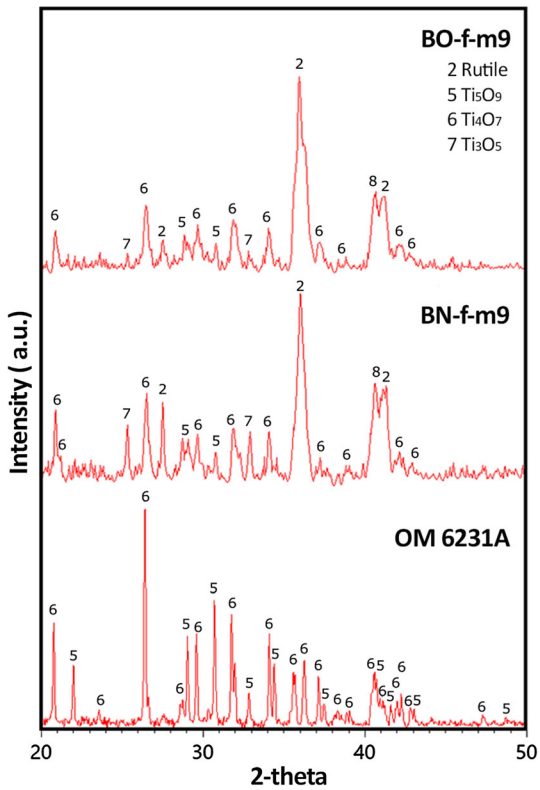

Fig. 6 XRD patterns of OM 6231A powder and the coatings sprayed from it

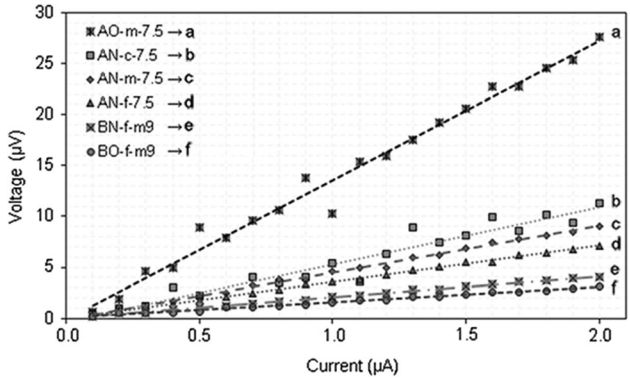

Fig. 7 Results of electrical resistance measured on coatings

Magnéli phases formation by reducing TiO_2 because of the use of hydrogen gas as reducing agent at temperatures higher than 1000 °C has been described by other authors through the Reaction 4 (Ref 16).

$$nTiO_2 + H_2 \rightarrow Ti_nO_{2n-1} + H_2O \quad \text{(Eq 4)}$$

The transformation of TiO_2 from the anatase phase in the US-RN agglomerated feedstock powder to both rutile and Magnéli phases, such as Ti_4O_7, in thermally sprayed coatings has been confirmed through the results of XPS analysis. This confirmation is based on the observation of shifting and broadening of the Ti2p high-resolution peaks, which correspond to the formation of several titanium oxides identified by the binding energy of the deconvoluted peaks. The peaks attributable to rutile, Ti_2O_3 and Ti_4O_7 as well as the absence of a peak located at 459.5 eV in the Ti $2p_{3/2}$ region, corresponding to Ti^{+4} of anatase phase indicate this. The Ti_4O_7 Magnéli phase has a unique structure in which the rutile blocks are interleaved with corundum-like Ti_2O_3 layers, and this leads to oxygen vacancy in the structure resulting in some lower valent and unsaturated Ti^{+3} (Ref 20, 41, 42). Furthermore, considering that the resolution depth of XPS analysis is typically only a few nanometers due to the inelastic mean free path (λ) of electrons with kinetic energies in the range of several hundreds of electron volts (eV), typically in the order of 10-25 Å (Ref 53), it is possible to conclude that the transformation from anatase to rutile and Magnéli phases occurs even on the surface of the coatings. This suggests that the particles on the surface, which experience the least heat accumulation during the thermal spraying process, undergo this transformation.

All the results mentioned above indicate that in both oxidizing and neutral flames, the transformation of TiO_2 from the anatase phase to rutile occurs at around 400 °C. Subsequently, at approximately 1000 °C, the anatase and rutile phases further transform into titanium suboxides, specifically Ti_nO_{2n-1}, according to Reaction 5.

$$nTiO_{2(Anatase)} \rightarrow nTiO_{2(Rutile)} + H_2 \rightarrow Ti_nO_{2n-1} + H_2O \quad \text{(Eq 5)}$$

In the above reaction, for the oxidizing flame, the value of n can be either 7 or 9. In the case of the neutral flame, when spraying with coarse or medium particle size fractions, the value of n is 7. However, when spraying with the fine particle size fraction in the neutral flame, the particles experience higher levels of heating, resulting in a greater reduction of TiO_2. This favors the formation of titanium suboxide with $n = 4$ and also leads to the appearance of Ti_3O in smaller quantities.

On the other hand, despite the absence of TiO_2 in the OM 6231A feedstock powder, its heating during the manufacturing of coatings in both the neutral and oxidizing flames leads to the production of TiO_2 in the rutile phase. The quantities of TiO_2 rutile phase generated are 8.8 wt.% for the neutral flame and 20.1 wt.% for the oxidizing flame. In the OM 6231A powder, the content of Ti_4O_7 Magnéli phase is measured at 58.5 ± 5.7 wt.%, while the content of Ti_5O_9 Magnéli phase is 41.5 ± 0.0 wt.%. Meanwhile, in the coating $B_{N\text{-}f\text{-}m9}$, sprayed using the neutral flame, these Magnéli phases are present in 52.7 ± 3.6 wt.% and 35.8 ± 3.1 wt.%, respectively, and in the sample $B_{O\text{-}f\text{-}m9}$, manufactured with the oxidizing flame, the content of those phases is 50.4 ± 1.4 wt.% and 28.2 ± 1.2 wt.%, respectively. The decrease in the percentages of Magnéli phases (Ti_4O_7 and Ti_5O_9) in the coatings compared to their presence in the feedstock powder indicates that the formation of the rutile phase occurred at the expense of these Magnéli phases. The higher oxidation of the Magnéli phases, leading to the formation of rutile in the coating sprayed using the oxidizing flame, could be attributed to the excess oxygen supplied to the primary zone of this flame.

Oxidation of Magnéli phases (Ti_4O_7 and Ti_5O_9) from OM 6231A feedstock powder to produce rutile in the thermally sprayed coatings has been confirmed through the analysis of the peaks identify by XPS, corresponding to Ti^{+3} in Ti_2O_3, Ti^{+4} of TiO_2 rutile phase, Ti^{+2} from TiO, and Ti^0 of metallic titanium. As indicated in the results section, the occurrence of peaks corresponding to Ti_2O_3 and rutile phase may be indicative of the presence of the Magnéli phase Ti_4O_7 (Ref 20, 41, 42). This would indicate that part of the rutile phase forms the intercalated blocks that give rise to the Magnéli phase, and another part corresponds to rutile as detected in the XRD analysis.

As mentioned earlier, the simultaneous presence of Ti^{3+} and Ti^{4+}, corresponding to Ti_2O_3 and TiO_2 rutile, respectively, can be indicative of the occurrence of Ti_4O_7. This is because the crystalline structure of the Ti_4O_7 Magnéli phase consists of rutile blocks interleaved with corundum-like Ti_2O_3 layers (Ref 20, 41, 42).

Based on the findings, it has been established that during the heating of Magnéli phases, the oxidation process is favored over further reduction of titanium suboxides. This suggests that the transformation from rutile to Magnéli phases in Reaction 5 is reversible, as demonstrated in Reaction 6.

$$Ti_nO_{2n-1} + H_2O \rightarrow nTiO_{2(Rutile)} + H_2 \quad \text{(Eq 6)}$$

In Reaction 6, the water vapor necessary for the oxidation of the Magnéli phases is supplied by the products of Reaction 3, which occur in the secondary zone of the flame. This secondary zone is generated after the primary zone, extending for a distance of 7.6 cm. To promote the flight of particles through the secondary zone after passing through the primary zone, the spraying distance was increased from 7.5 cm for the coatings manufactured with the US-RN powder to 9 cm for those manufactured using the OM 6231A feedstock material. The oxidation of Magnéli phases sprayed using an oxyacetylene flame has been previously reported by other authors (Ref 30).

The results of electrical resistance measurements (R) demonstrate that as the percentage of more reduced Magnéli phases increases in the coatings, the electrical conductance (1/R) also increases. This confirms the high conductivity of Ti_4O_7 and Ti_5O_9 phases, as previously reported by other authors (Ref 4, 54). The structure of Ti_4O_7, which consists of rutile blocks interleaved with corundum-like Ti_2O_3 layers, creates oxygen vacancies within the crystal lattice. These oxygen vacancies can cause contraction in the lattice, leading to overlapping of the 3d orbitals of titanium. This overlap broadens the conduction band, facilitating the conduction of electric charge. Hence, the presence of oxygen vacancies in Ti_4O_7 contributes to its high electrical conductivity (Ref 20, 41).

The electrical conductance of the coatings thermally sprayed from the OM 6231A powder is primarily driven by the presence of the TiO phase, as detected by XPS analysis. The TiO phase exhibits conductivity values that are ≈ 3 times higher than that of Ti_4O_7 and 9 times higher than that of Ti_5O_9 Magnéli phases. This indicates that TiO plays a significant role in enhancing the electrical conductivity of the coatings (Ref 4).

5. Conclusions

Formation and transformation of Magnéli phases during ceramic coating manufacturing by flame spraying from feedstock powders containing TiO_2 as anatase phase and Magnéli phases are analyzed in this paper. Coatings fabrication was executed on a silico-aluminous ceramic substrate using both the neutral and oxidizing flames of an oxyacetylene thermal spraying process.

The results allow us to conclude that it is possible to synthesize Magnéli phases through the flame spraying process using TiO_2 powders in the anatase phase. Both neutral and oxidizing flames can be utilized, with the neutral flame achieving a higher degree of reduction, especially when using smaller particles. The transformation of TiO_2 to Ti_nO_{2n-1} Magnéli phases is reversible in both neutral and oxidizing flames, resulting in the production of TiO_2 in the rutile phase. Furthermore, the transformation of Ti_nO_{2n-1} to TiO_2 is more effective in the oxidizing flame. Ti_4O_7, synthesized from agglomerated nanoparticles of anatase, as well as the remaining Ti_4O_7 from OM 6231A powder, plays a significant role in reducing the electrical resistance of the coatings. Additionally, the presence of Ti_5O_9 and TiO also contributes to the enhancement of electrical conductivity in the thermally sprayed coatings from OM 6231A powder. Despite TiO being present in smaller quantities, its higher conductivity greatly reduces the electrical resistance of the coatings.

Acknowledgments

Authors thank to both Ministerio de Ciencia and Tecnología e Innovación de Colombia—Minciencias, for the financial support given to the proposal 12167775759 under the contract 657 of 2018 that allowed the realization of this research, as well as to CODI of Universidad de Antioquia, by the support given to project PR 21-1-03.

Funding

Open Access funding provided by Colombia Consortium.

References

1. J.R. Smith, F.C. Walsh, and R.L. Clarke, Electrodes Based on Magnéli Phase Titanium Oxides: The Properties and Applications of Ebonex® Materials, *J. Appl. Electrochem.Electrochem.*, 1998, **28**(10), p 1021-1033. https://doi.org/10.1023/A:1003469427858
2. A.F. Arif, R. Balgis, T. Ogi, F. Iskandar, A. Kinoshita, K. Nakamura, and K. Okuyama, Highly Conductive Nano-Sized Magnéli Phases Titanium Oxide (TiOx), *Sci. Rep.*, 2017, **7**(1), p 1-9. https://doi.org/10.1038/s41598-017-03509-y
3. C. Tang, D. Zhou, and Q. Zhang, Synthesis and Characterization of Magneli Phases: Reduction of TiO_2 in a Decomposed NH_3 Atmosphere, *Mater. Lett.*, 2012, **79**, p 42-44. https://doi.org/10.1016/j.matlet.2012.03.095
4. B. Xu, H.Y. Sohn, Y. Mohassab, and Y. Lan, Structures, Preparation and Applications of Titanium Suboxides, *RSC Adv.*, 2016, **6**(83), p 79706-79722. https://doi.org/10.1039/c6ra14507h
5. M. Domaschke, X. Zhou, L. Wergen, S. Romeis, M.E. Miehlich, K. Meyer, W. Peukert, and P. Schmuki, Magnéli-Phases in Anatase Strongly Promote Cocatalyst-Free Photocatalytic Hydrogen Evolution, *ACS Catal.Catal.*, 2019, **9**(4), p 3627-3632. https://doi.org/10.1021/acscatal.9b00578
6. J.M. Coronado, F. Fresno, M.D. Hernández-Alonso, and R. Portela, Design of Advanced Photocatalytic Materials for Energy and Environmental Applications, *Green Energy Technol.*, 2013 https://doi.org/10.1007/978-1-4471-5061-9
7. G. Wang, Y. Liu, J. Ye, and W. Qiu, Synthesis, Microstructural Characterization, and Electrochemical Performance of Novel Rod-like ti_4o_7 Powders, *J. Alloys Compd.*, 2017, **704**, p 18-25. https://doi.org/10.1016/j.jallcom.2017.02.022
8. X. Yan, Y. Li, and T. Xia, Black Titanium Dioxide Nanomaterials in Photocatalysis, *Int. J. PhotoenergyPhotoenergy*, 2017 https://doi.org/10.1155/2017/8529851
9. X. Li, A.L. Zhu, W. Qu, H. Wang, R. Hui, L. Zhang, and J. Zhang, Magneli Phase Ti_4O_7 Electrode for Oxygen Reduction Reaction and its Implication for Zinc-Air Rechargeable Batteries, *Electrochim. Acta. Acta*, 2010, **55**(20), p 5891-5898. https://doi.org/10.1016/j.electacta.2010.05.041
10. H. Hu, Y. Lin, and Y.H. Hu, Phase Role of White TiO_2 Precursor in its Reduction to Black TiO_2, *Phys. Lett. Sect. A Gen. At. Solid State Phys.*, 2019, **383**(24), p 2978-2982.
11. M. Toyoda, T. Yano, B. Tryba, S. Mozia, T. Tsumura, and M. Inagaki, Preparation of Carbon-Coated Magneli Phases $TinO_2n$-1 and Their Photocatalytic Activity under Visible Light, *Appl. Catal. B Environ.Catal. B Environ.*, 2009, **88**(1-2), p 160-164. https://doi.org/10.1016/j.physleta.2019.06.025
12. M. Pylnev and M.S. Wong, Comparative Study of Photocatalytic Deactivation of Pure and Black Titania Thin Films, *J. Photochem. Photobiol. A Chem.*, 2019, **378**(February), p 125-130. https://doi.org/10.1016/j.jphotochem.2019.04.020
13. F.C. Walsh and R.G.A. Wills, The Continuing Development of Magnéli Phase Titanium Sub-Oxides and Ebonex® Electrodes, *Electrochim. Acta. Acta*, 2010, **55**(22), p 6342-6351. https://doi.org/10.1016/j.electacta.2010.05.01
14. P.C.S. Hayfield, Development of a New Material-Monolithic Ti_4O_7 Ebonex® Ceramic, *R. Soc. Chem.*, 2002 https://doi.org/10.1017/CBO9781107415324.004
15. X. Chen, L. Liu, and F. Huang, Black Titanium Dioxide (TiO_2) Nanomaterials, *Chem. Soc. Rev.*, 2015, **44**(7), p 1861-1885. https://doi.org/10.1039/c4cs00330f
16. S.-S. Huang, Y.-H. Lin, W. Chuang, P.-S. Shao, C.-H. Chuang, J.-F. Lee, M.-L. Lu, Y.-T. Weng, and N.-L. Wu, Synthesis of High-Performance Titanium Sub-Oxides for Electrochemical Applications using Combination of Sol-Gel and Vacuum-Carbothermic Processes, *ACS Sustain. Chem. Eng.*, 2018, **6**(3), p 3162-3168. https://doi.org/10.1021/acssuschemeng.7b03189
17. S. Conze, I. Veremchuk, M. Reibold, B. Matthey, A. Michaelis, Y. Grin, and I. Kinski, Magnéli Phases Ti_4O_7 and Ti_8O_{15} and Their Carbon Nanocomposites via the Thermal Decomposition-Precursor Route, *J. Solid State Chem.*, 2015, **229**, p 235-242. https://doi.org/10.1016/j.jssc.2015.04.037
18. K.E. Hurst, J.M. Luther, C. Ban, and S.T. Christensen, Nanomaterials for Energy Applications, *Mater. Chem. Sci. Technol. Protoc. Ind. Innov.*, 2017, **13**(42), p 505-517. https://doi.org/10.1002/9783527800308.ch28
19. A. Kumar, N.H. Barbhuiya, and S.P. Singh, Chemosphere Magnéli Phase Titanium Sub-Oxides Synthesis, Fabrication and its Application for Environmental Remediation: Current Status and Prospect, *Chemosphere*, 2022, **307**(P2), p 135878. https://doi.org/10.1016/j.chemosphere.2022.135878
20. M. Liu, S. Jhulki, Z. Sun, A. Magasinski, C. Hendrix, and G. Yushin, Atom-Economic Synthesis of Magnéli Phase Ti_4O_7 Microspheres for Improved Sulfur Cathodes for Li–S Batteries, *Nano Energy*, 2021, **79**, p 105428. https://doi.org/10.1016/j.nanoen.2020.105428
21. R. Zhu, Y. Liu, J. Ye, and X. Zhang, Magnéli Phase Ti_4O_7 Powder from Carbothermal Reduction Method: Formation, Conductivity and Optical Properties, *J. Mater. Sci. Mater. Electron.*, 2013, **24**(12), p 4853-4856. https://doi.org/10.1007/s10854-013-1487-5
22. M. Wajid Shah, Y. Zhu, X. Fan, J. Zhao, Y. Li, S. Asim, and C. Wang, Facile Synthesis of Defective TiO_2-x Nanocrystals with High Surface Area and Tailoring Bandgap for Visible-Light Photocatalysis, *Sci. Rep.*, 2015, **5**(1), p 15804.
23. B. Babić, J. Gulicovski, L. Gajić-Krstajić, N. Elezović, V.R. Radmilović, N.V. Krstajić, and L.M. Vračar, Kinetic Study of the Hydrogen Oxidation Reaction on Sub-Stoichiometric Titanium Oxide-Supported Platinum Electrocatalyst in Acid Solution, *J. Power Sour.*, 2009, **193**(1), p 99-106. https://doi.org/10.1016/j.jpowsour.2008.11.142
24. L. Pawlowski, The Science and Engineering of Thermal Spray Coatings. 2nd Edn, Wiley, 2008, https://doi.org/10.1002/9780470754085
25. P. Ctibor and M. Hrabovský, Plasma Sprayed TiO_2: The Influence of Power of an Electric Supply on Particle Parameters in the Flight and Character of Sprayed Coating, *J. Eur. Ceram. Soc.*, 2010, **30**(15), p 3131-3136. https://doi.org/10.1016/j.jeurceramsoc.2010.05.029
26. P. Ctibor, V. Štengl, I. Píš, T. Zahoranová, and V. Nehasil, Plasma Sprayed TiO_2: The Influence of Power of an Electric Supply on Relations among Stoichiometry, Surface State and Photocatalytic Decomposition of Acetone, *Ceram. Int.*, 2012, **38**(4), p 3453-3458. https://doi.org/10.1016/j.ceramint.2011.12.058
27. D. Jaramillo Raquejo, C.C. Palacio, and H. Ageorges, Study of APS and Conventional Sintering Parameters for the Manufacture of TiO_2 Targets for PAPVD, *J. Phys. Conf. Ser.*, 2019, **1247**(1), p 1-11.
28. L.M. Berger, Titanium Oxide-New Opportunities for an Established Coating Material, *Proc. Int. Therm. Spray Conf.*, 2004, (April), p. 934-945, https://doi.org/10.31399/asm.cp.itsc2004p0934
29. B. Xu, D. Zhao, H.Y. Sohn, Y. Mohassab, B. Yang, Y. Lan, and J. Yang, Flash Synthesis of Magnéli Phase ($TinO_2n$-1) Nanoparticles by Thermal Plasma Treatment of H_2TiO_3, *Ceram. Int.*, 2018, **44**(4), p 3929-3936. https://doi.org/10.1016/j.ceramint.2017.11.184
30. G. Peña-Rodríguez, H.J. Dulce-moreno, and F. Vargas-Galvis, Recubrimientos de TiO_2 Sobre Sustratos de Arcilla Roja Usando Proyección Térmica Oxiacetilénica (TiO_2 Coatings on Red Clay

Substrates Using Oxyacetylene Thermal Spraying), *Rev. Latinoam. Metal. Mater.*, 2018, **38**(1), p 7-8.
31. J.A. Árias, F.M. Hurtado, F. Vargas, G. Estrada, E. Cadavid, M.R. Ortiz, and F. Vargas, Pelletisation by Tumbling as an Alternative Method of Agglomerating Nanometric Particles for Use as Feedstock in Bi-Modal Structured Flame-Sprayed Ceramic Coatings, *Ceram. Int.*, 2019, **45**(16), p 20936-20944. https://doi.org/10.1016/j.ceramint.2019.07.083
32. Oerlikon Metco, Thermal Spray Materials Guide–April 2015, (2015), https://www.ahtstlab.com/wp-content/uploads/2021/05/ThermalSprayMaterialsGuide.pdf. Accessed 15 Sept 2023
33. Oerlikon Metco, Material Manufacturing Technology, (2023), https://www.oerlikon.com/metco/en/solutions-technologies/technology/material-manufacturing-technology/#:~:text=Slurries containing the constituents for, produce cemented or tungsten carbides. Accessed 15 Sept 2023
34. I.A. Lira-Hernandez, F.R. Barrientos-Hernandez, M. Perez-Labra, A.M. Gracia-Mercado, and J.A. Romero-Serrano, Comments about Rietveld Analysis and Tolerance Factor: Y Doped $BaTiO_3$, *Preprint*, 2016, **2**(October), p. 1-11, https://doi.org/10.20944/preprints201610.0126.v1
35. S.Y. Purwaningsih, N. Rosidah, M. Zainuri, T. Triwikantoro, S. Pratapa, and D. Darminto, Comparation of x-ray Diffraction Pattern Refinement using Rietica and MAUD of ZnO Nanoparticles and Nanorods, *J. Phys. Conf. Ser.*, 2019 https://doi.org/10.1088/1742-6596/1153/1/012070
36. A. Fujishima, X. Zhang, and D.A. Tryk, TiO_2 Photocatalysis and Related Surface Phenomena, *Surf. Sci. Rep.*, 2008, **63**(12), p 515-582. https://doi.org/10.1016/j.surfrep.2008.10.001
37. A.S. Barnard and L.A. Curtiss, Prediction of TiO_2 Nanoparticle Phase and Shape Transitions Controlled by Surface Chemistry, *Nano Lett.*, 2005, **5**(7), p 1261-1266. https://doi.org/10.1021/nl050355m
38. K. Piler, C. Bahrim, S. Twagirayezu, and T.J. Benson, Chapter Two-Lattice Disorders of TiO_2 and Their Significance in the Photocatalytic Conversion of CO_2, *Adv. Catal.Catal.*, 2020, **66**, p 109-233. https://doi.org/10.1016/BS.ACAT.2020.09.001
39. H. Zhang and J.F. Banfield, Thermodynamic Analysis of Phase Stability of Nanocrystalline Titania, *J. Mater. Chem.*, 1998, **8**(9), p 2073-2076. https://doi.org/10.1039/a802619j
40. P.L. Fauchais, J.V.R. Heberlein, and M.I. Boulos, Thermal Spray Fundamentals, *Springer Science+Business Media*, Springer Science+Business Media New York 2014, (2014), https://doi.org/10.1007/978-0-387-68991-3
41. P. Geng, J. Su, C. Miles, C. Comninellis, and G. Chen, Highly-Ordered Magnéli Ti_4O_7 Nanotube Arrays as Effective Anodic Material for Electro-Oxidation, *Electrochim. Acta. Acta*, 2015, **153**, p 316-324. https://doi.org/10.1016/j.electacta.2014.11.178
42. P. Geng and G. Chen, Magnéli Ti_4O_7 Modified Ceramic Membrane for Electrically-Assisted Filtration with Antifouling Property, *J. Memb. Sci.*, 2016, **498**, p 302-314. https://doi.org/10.1016/j.memsci.2015.07.055
43. S. Tominaka, Y. Tsujimoto, Y. Matsushita, and K. Yamaura, Synthesis of Nanostructured Reduced Titanium Oxide: Crystal Structure Transformation Maintaining Nanomorphology, *Angew. Chem. Int. Ed.. Chem. Int. Ed.*, 2011, **50**, p 7418-7421. https://doi.org/10.1002/anie.201101432
44. W. Xie, R. Li, and Q. Xu, Enhanced photocatalytic activity of Se-doped TiO_2 under visible light irradiation, *Sci. Rep.*, 2018, **8**(1), p 8752. https://doi.org/10.1038/s41598-018-27135-4
45. B. C. M., x-ray Photoelectron Spectroscopy (XPS) Refernce Pages: Titanium, *Xpsfitting*, (2021), http://www.xpsfitting.com/2008/09/titanium.html. Accessed 14 July 2023, p 1
46. J. Yao, J. Shao, H. He, and Z. Fan, Optical and Electrical Properties of TiOx Thin Films Deposited by Electron Beam Evaporation, *Vacuum*, 2007, **81**(9), p 1023-1028. https://doi.org/10.1016/j.vacuum.2006.11.002
47. Q. Zhang and C. Li, High Temperature Stable Anatase Phase Titanium Dioxide Films Synthesized by Mist Chemical Vapor Deposition, *Nanomaterials*, 2020, **10**(5), p 1-8. https://doi.org/10.3390/nano10050911
48. D.A.H. Hanaor and C.C. Sorrell, Review of the Anatase to Rutile Phase Transformation, *J. Mater. Sci.*, 2011, **46**(4), p 855-874. https://doi.org/10.1007/s10853-010-5113-0
49. I. Glassman, R.A. Yetter, and N.G. Glumac, Combustion, Fifth Edit, *Acad. Press*, 2015 https://doi.org/10.1016/B978-0-12-407913-7.03001-2
50. J. Henao, C.A. Poblano-Salas, F. Vargas, A.L. Giraldo-Betancur, J. Corona-Castuera, and O. Sotelo-Mazón, Principles and Applications of Thermal Spray Coatings, (Pensilvania), *IGI Glob.*, 2021 https://doi.org/10.4018/978-1-7998-4870-7.ch002
51. E.H.C. Iglesias, C.P. Velásquez, and F.V. Galvis, Estudio de Llamas Oxiacetilénicas Usadas en la Proyección Térmica, *Rev. Colombiana de Mater.*, 2016, **9**, p 15-26.
52. F. Vargas, E. Restrepo, J.E. Rodríguez, F. Vargas, L. Arbeláez, P. Caballero, J. Arias, E. López, G. Latorre, and G. Duarte, Solid-State Synthesis of Mullite from Spent Catalysts for Manufacturing Refractory Brick Coatings, *Ceram. Int.*, 2018 https://doi.org/10.1016/j.ceramint.2017.11.044
53. G. Greczynski and L. Hultman, X-Ray Photoelectron Spectroscopy: Towards Reliable Binding Energy Referencing, *Prog. Mater. Sci.. Mater. Sci.*, 2020, **107**, p 100591. https://doi.org/10.1016/j.pmatsci.2019.100591
54. A.A. Gusev, E.G. Avvakumov, A.Z. Medvedev, and A.I. Masliy, Ceramic Electrodes Based on Magneli Phases of Titanium Oxides, *Sci. Sinter.*, 2007, **39**, p 51-57. https://doi.org/10.1016/j.ceramint.2017.11.044